Renewable Energy 209 (2023) 27–41

Contents lists available at ScienceDirect

Renewable Energy

journal homepage: www.elsevier.com/locate/renene

Turbulence in waked wind turbine wakes: Similarity and empirical formulae

Yi Zhang [a,b,d], Zhaobin Li [a,b], Xiaohao Liu [a,b], Fotis Sotiropoulos [c], Xiaolei Yang [a,b,*]

[a] The State Key Laboratory of Nonlinear Mechanics, Institute of Mechanics, Chinese Academy of Sciences, Beijing, 100190, China
[b] School of Engineering Sciences, University of Chinese Academy of Sciences, Beijing, 100049, China
[c] Department of Mechanical and Nuclear Engineering, Virginia Commonwealth University, Richmond, 23284, VA, USA
[d] College of Civil Engineering and Mechanics, Lanzhou University, Lanzhou, 730000, China

ARTICLE INFO

Keywords:
Wind turbine wake
Similarity
Empirical formulae
Reynolds normal stress

ABSTRACT

Turbulence of wind turbine wakes increases the power fluctuations and dynamic loads of downwind turbines. In this work, we analyze the large-eddy simulation (LES) data of the Horns Rev wind farm, and find that the streamwise variations of the Reynolds normal stresses in the wakes of the waked wind turbines located in different rows collapse well with each other for both rise and decay portions when they are normalized using the maxima. Empirical formulae in the form of a power function are then proposed to describe the streamwise variations of the Reynolds normal stresses for different blade spanwise positions. Notably, linear relations are observed between the exponent and the coefficient. The LES data of the two tandem wind turbine cases with different inflows and turbine spacings are then employed to test the proposed empirical formulae. The tests show that the empirical formulae can capture the downstream variations of the Reynolds normal stresses especially for the streamwise component.

1. Introduction

Waked wind turbines generate power with high-amplitude fluctuations and bear high dynamic loads because of the high turbulence intensity in wind turbine wakes [1,2]. Thus understanding the dynamics of wake turbulence and developing engineering models for a fast prediction of its downstream evolution are essential for advancing wind technologies to better account for the effect of wake turbulence. The wake of a wind turbine can be divided into two regions, the near wake within 2–4 rotor diameters turbine downstream, where the characteristics are directly affected by the turbine and the wake is featured by three-dimensional flow structures (e.g., tip and hub vortices) [3], and the far wake, where the wind turbine condition is less significant and the wake is featured by a low-frequency, large-scale meandering motion [4]. The far wake has a direct influence on downstream wind turbines [5], and its turbulence characteristics are the focus of this work.

Engineering wake models [3,6], because of their computational efficiency, play a vital role in the design and control of wind farms. In the literature, different empirical formulae for the added turbulence intensity $\Delta I = (I^2 - I_a^2)^{1/2}$ (where $I = \sigma_u/U$, σ_u is the standard deviation of the streamwise velocity fluctuations, U is the incoming wind speed, and I_a is the ambient turbulence intensity) have been developed, which are often in the form of a power function of the turbine downstream distance x (e.g., $\Delta I = A(x/D)^B$, where D is the rotor diameter, and A and B are the model coefficient and the decay exponent depending on the thrust coefficient, the inflow turbulence intensity and other factors.). For instance, a decay of ΔI following $x^{-0.5}$ was given by Högström et al. [7] for $x \in [2D, 10D)$. Crespo and Hernandez [8] obtained the expression, $\Delta I = 0.73a^{0.8325} I_a^{-0.0325}(x/D)^{-0.32}$, in which a is the axial induction factor. In the expression proposed by Quarton [5], the thrust coefficient C_T is employed instead of a, which is in the form of $\Delta I = 4.8C_T^{0.7} I_a^{0.68}(x/x_N)^{-0.57}$ (where x_N is the near wake length to be specified). Based on the classical wake theory of Schlichting, Larsen et al. [5,9] proposed an expression in the form of $\Delta I = 0.29\sqrt{1-\sqrt{(1-C_T)}}(x/D)^{-1/3}$. As for the decay exponent, Neunaber et al. [10] found that it changes from the beginning of the decay to the far wake. For wind turbine clusters, it was shown that the power law also applies but with a smaller decay exponent [5].

Recently, Ishihara and Qian [11] and Li et al. [12] developed models to account for the variation of the added turbulence intensity in the blade spanwise direction. It is noticed that most existing engineering expressions only describe the decay portion of the turbulence intensity, focusing on the streamwise component without considering other two

* Corresponding author at: The State Key Laboratory of Nonlinear Mechanics, Institute of Mechanics, Chinese Academy of Sciences, Beijing, 100190, China.
E-mail address: xyang@imech.ac.cn (X. Yang).

https://doi.org/10.1016/j.renene.2023.03.068
Received 16 October 2022; Received in revised form 15 February 2023; Accepted 16 March 2023
Available online 22 March 2023

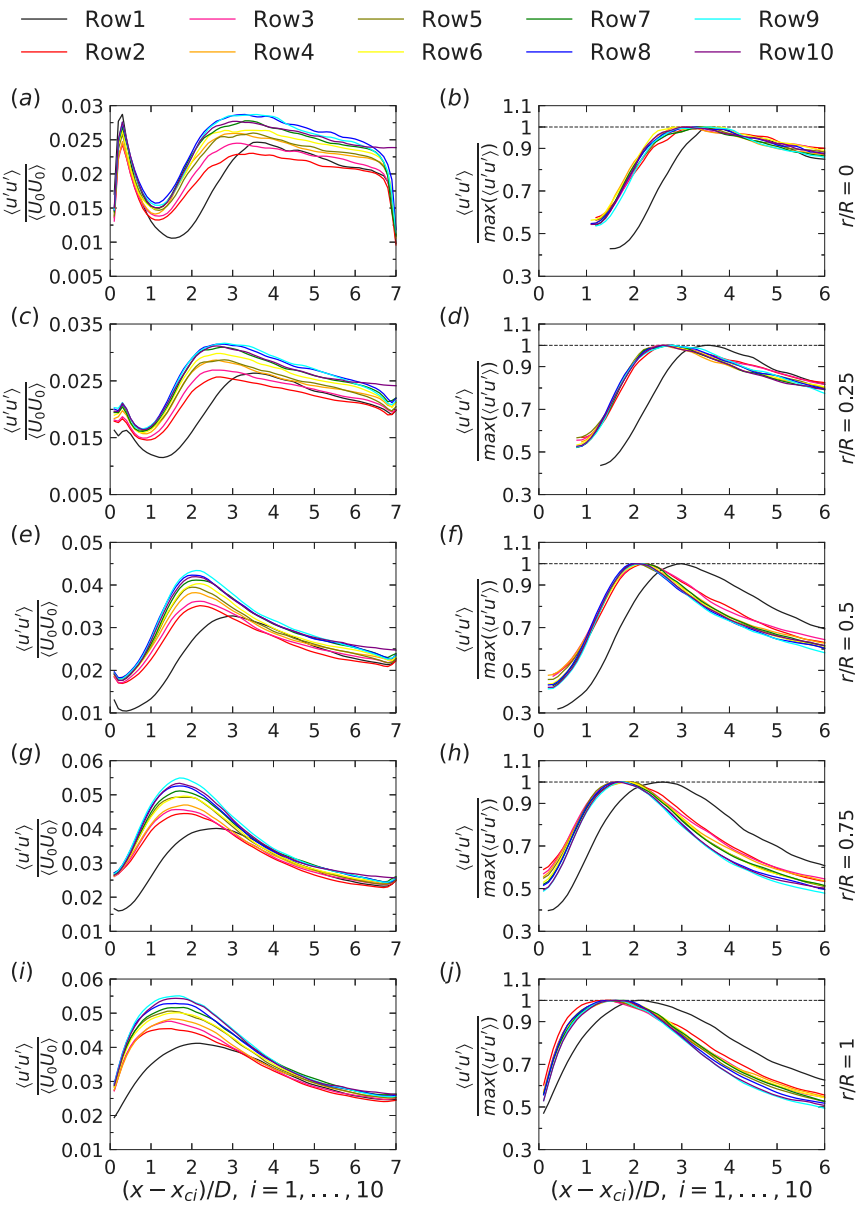

Fig. 1. Downstream variations of the streamwise Reynolds normal stress for Row1-10 at different blade spanwise positions. In the left subfigures (a,c,e,g,i) the stresses are normalized using U_0, while in the right subfigures (b,d,f,h,j) are normalized by the corresponding maximum in the range of $1D - 6D$ turbine downstream. The horizontal axis shows the downstream distance from the corresponding upstream turbine.

components. Furthermore, none of them properly takes into account the effect of oncoming wakes.

Similarity is critical for developing empirical formulae for wake turbulence. Self-similarity has been employed for developing the analytical models for the velocity deficit [13] and the added turbulence intensity [14]. In addition to the self-similarity, similarities between wind turbine wakes under different conditions were also observed, for instance, for different wind turbine designs [15], different yaw angles [16], and different turbine spacings for waked wind turbines [17].

In this paper, we examine the similarity of different components of Reynolds normal stresses for wind turbine wakes in a wind farm, propose empirical formulae for the downwind variations of Reynolds normal stresses based on the observed similarity, and evaluate the proposed formulae using the wake data from LES of two tandem wind turbines with different turbine spacings.

The key innovation of this study is the discovery of similarities in the rise and decay portions of the Reynolds normal stresses. This similarity suggests that the normalization factors employed, i.e., the maximum values of Reynolds normal stresses and the rotor diameter, define the streamwise development of turbulence generated by the wake. Additionally, the empirical formulae proposed for various blade spanwise locations are found to be applicable to different wind turbine designs, inflows, and turbine spacings.

The rest of the paper is organized as follows. The numerical method employed for LES and the LES data are described in Section 2. The

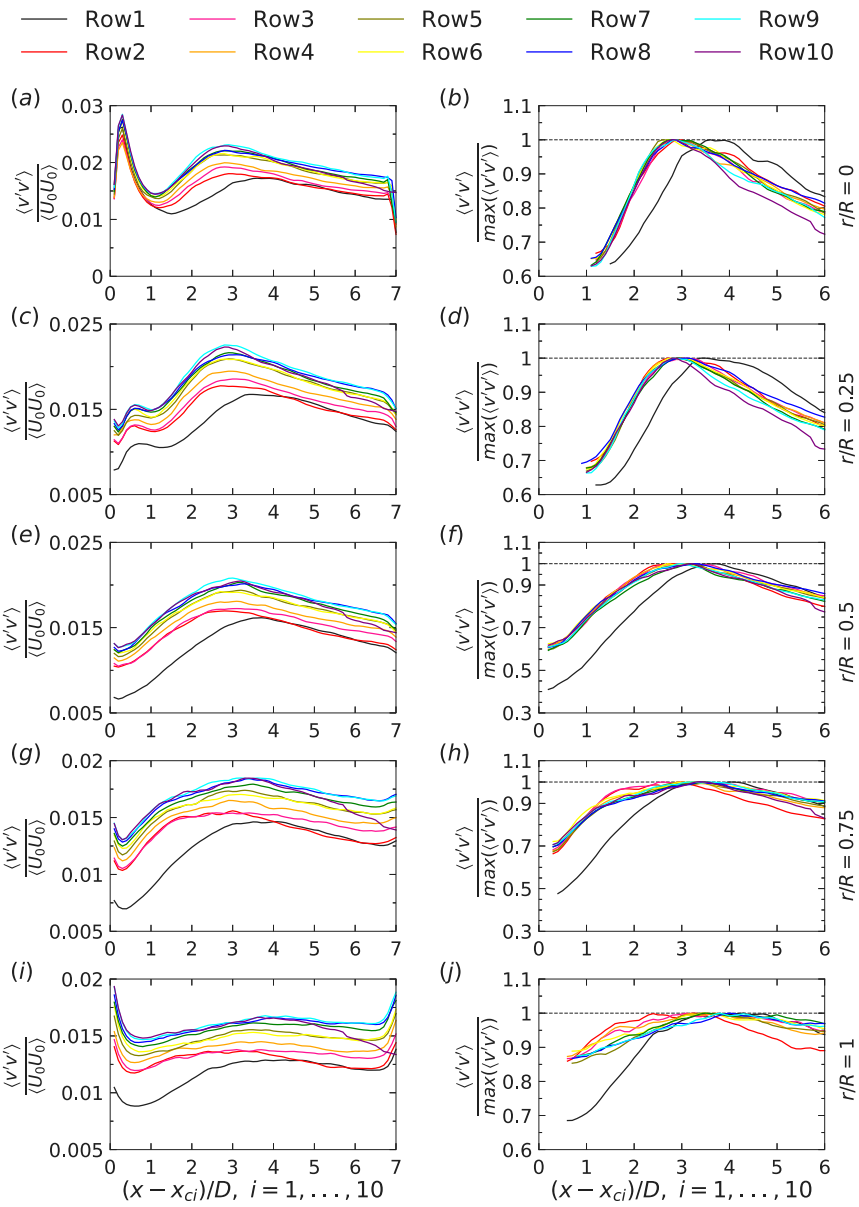

Fig. 2. Downstream variations of the spanwise Reynolds normal stress for Row1-10 at different blade spanwise positions. In the left subfigures (a,c,e,g,i) the stresses are normalized using U_0, while in the right subfigures (b,d,f,h,j) are normalized by the corresponding maximum in the range of $1D - 6D$ turbine downstream. The horizontal axis shows the downstream distance from the corresponding upstream turbine.

analysis of similarity of Reynolds normal stresses and the proposed empirical formulae are presented in Section 3. At last, conclusions are drawn in Section 4.

2. LES data of the Horns Rev wind farm and two tandem wind turbine cases

In this section, the LES cases of the Horns Rev wind farm and two tandem wind turbines are briefly described in Sections 2.2 and 2.3, respectively, in which the turbulence statistics from the former case are systematically analyzed and the data from the latter cases are employed for testing the empirical formulae obtained using the data from the former case.

2.1. The virtual flow simulator code

The VFS-Wind code [18,19] employed for carrying out the LES cases is described in this section. The governing equations are the three-dimensional filtered Navier–Stokes equations in curvilinear coordinates as follows:

$$J\frac{\partial U^i}{\partial \xi^i} = 0, \tag{1}$$

$$\frac{1}{J}\frac{\partial U^i}{\partial t} = \frac{\xi_l^i}{J}\left(-\frac{\partial\left(U^j u_l\right)}{\partial \xi^j} + \frac{\mu}{\rho}\frac{\partial\left(\frac{g^{jk}}{J}\frac{\partial u_l}{\partial \xi^k}\right)}{\partial \xi^j} - \frac{1}{\rho}\frac{\partial\left(\frac{\xi_l^j p}{J}\right)}{\partial \xi^j} - \frac{1}{\rho}\frac{\partial \tau_{lj}}{\partial \xi^j} + f_l\right), \tag{2}$$

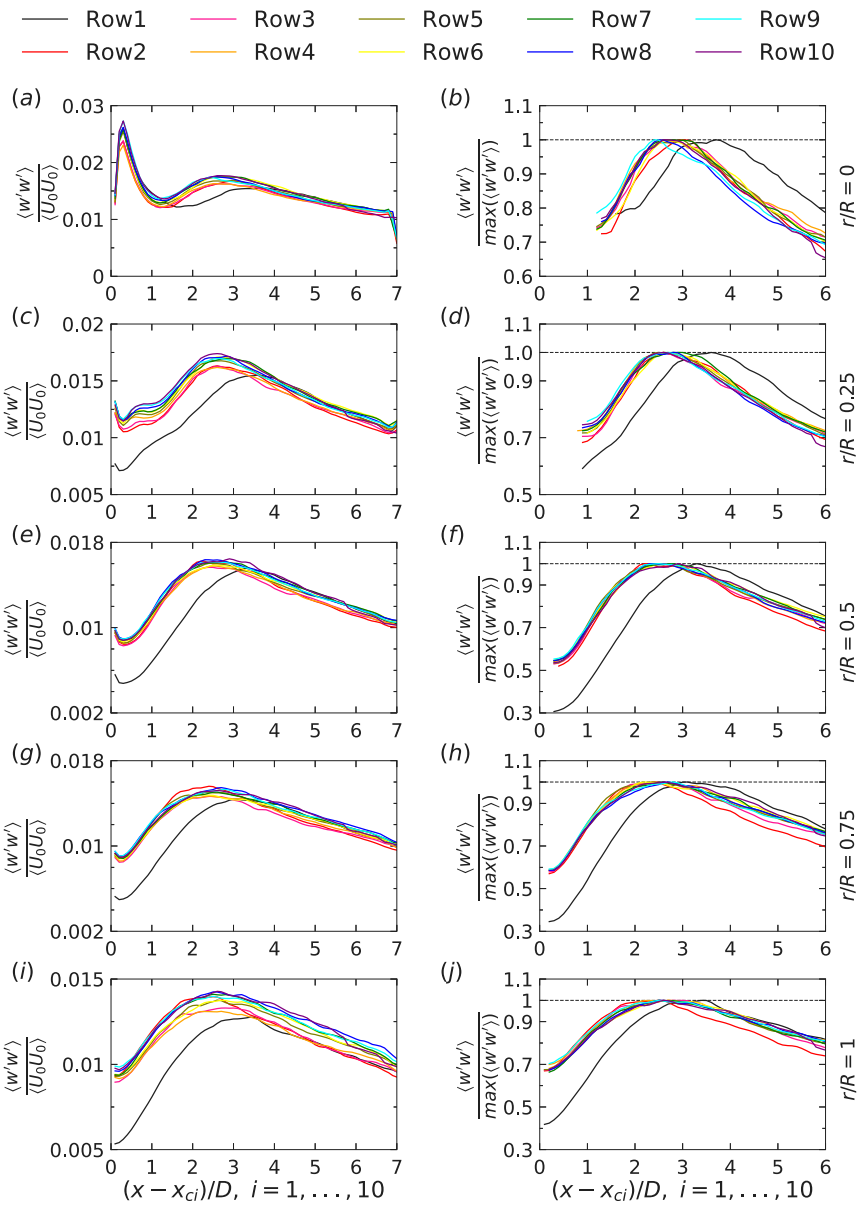

Fig. 3. Downstream variations of the vertical Reynolds normal stress for Row1-10 at different blade spanwise positions. In the left subfigures (a,c,e,g,i) the stresses are normalized using U_0, while in the right subfigures (b,d,f,h,j) are normalized by the corresponding maximum in the range of $1D - 6D$ turbine downstream. The horizontal axis shows the downstream distance from the corresponding upstream turbine.

where $i, j, k, l = 1, 2, 3$, ξ^i are the curvilinear coordinates, $\xi_l^i = \frac{\partial \xi_i}{\partial x_l}$ is the transformation metrics, J is the Jacobian of the geometric transformation, $U^i = (\xi_l^i / J) u_l$ is the contravariant volume flux, u_i is the ith component of velocity vector in the Cartesian coordinates, μ is the dynamic viscosity, $g^{jk} = \tau_l^j \tau_l^k$ is the components of the contravariant metric tensor, p is the pressure, f_l are the body forces resulted from the actuator surface models for wind turbine blades and nacelle [19], and τ_{ij} is the sub-grid stress (SGS) tensor modeled using the dynamic Smagorinsky model [20].

The actuator surface models are employed for parameterizing the aerodynamics of turbine blades and nacelle [19]. In the actuator surface model for blades, the blade geometry is represented by an actuator surface of zero thickness, which is formed by the chords at different blade spanwise locations. The drag and lift at each blade spanwise location are computed based on the blade element method. The obtained drag and lift are then uniformly distributed in the chordwise direction. In the actuator surface model for nacelle, the forces are distributed on the nacelle surface. The normal force is determined by satisfying the non-penetration boundary condition. The tangential force is computed using a specified force coefficient and the incoming wind speed. In both models, the grid nodes discretizing the actuator surfaces in general do not coincide with the background grid nodes. The smoothed discrete

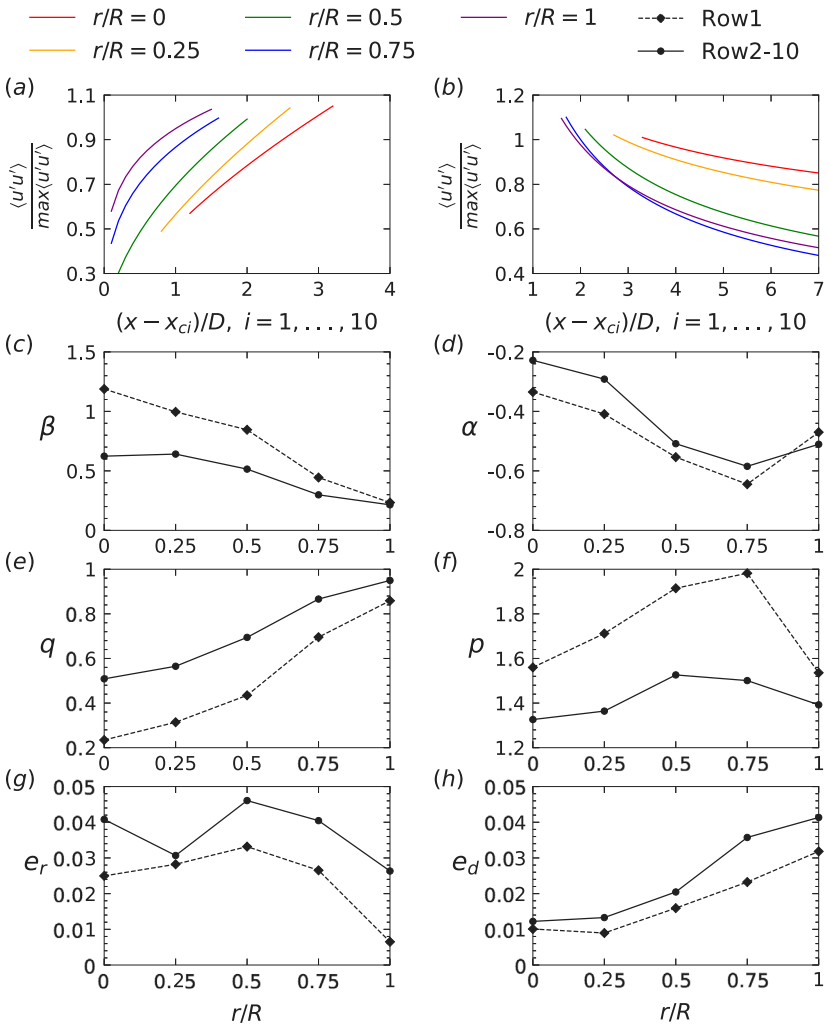

Fig. 4. Fitting results for the streamwise Reynolds normal stress for (a,b) the fitted curves for Row2-10, (c,d) exponents, (e,f) coefficients, and (g,h) errors. (a,c,e,g) are for the rise and (b,d,f,h) are for the decay, respectively.

delta function proposed by Yang et al. [21] is employed for transferring the information between the two sets of grids.

The governing equations are discretized in space using a second-order accurate central differencing scheme and advanced in time using the fractional step method [22]. A matrix-free Newton–Krylov method [23] and the Generalized Minimal Residual (GMRES) method along with an algebraic multi-grid acceleration [24] are employed for solving the momentum equation and the pressure Poisson equation, respectively.

2.2. Horns Rev wind farm case

The similarity of the Reynolds normal stresses is analyzed using the LES data of the Horns Rev (HR) offshore wind farm [15]. The wind farm is composed of 80 Vestas V80-2 MW turbines of diameter $D = 80$ m and hub height $z_h = 70$ m, placed in a parallelogram pattern of 10 rows (expressed as Row1, . . . , Row10 in the following) with 8 wind turbines in each row. The streamwise and spanwise wind turbine spacings are both $7D$. The height of the atmospheric boundary layer is set to $\delta = 1000$ m. The undisturbed incoming wind speed U_0 at hub height is slightly different at different spanwise positions, with the spanwise-averaged one 8 m/s. The tip speed ratio is 7.5 for all wind turbines. The sea surface is modeled with the logarithmic law for rough wall with roughness length $k_0 = 0.0001$ m. The free-slip boundary is applied at the top and spanwise boundaries. The size of the computational domain is $70D \times 54D \times 12.5D$ in the streamwise, spanwise and vertical directions with the corresponding grid cells $1561 \times 1470 \times 152$.

Due to the non-rectangular layout of the wind farm, the background grid nodes of the same streamwise index do not correspond to the same wind turbine downstream location $x - x_{ci}$, where x_{ci} is the streamwise coordinate of the wind turbine (i represents the row index). Therefore, the data are interpolated to obtain the quantities at the same wind turbine downstream locations for the eight wind turbines in the same row.

2.3. Two tandem wind turbine cases

This dataset consist of the LES data for a simplified case with only two wind turbines arranged in tandem [17]. Four different turbine

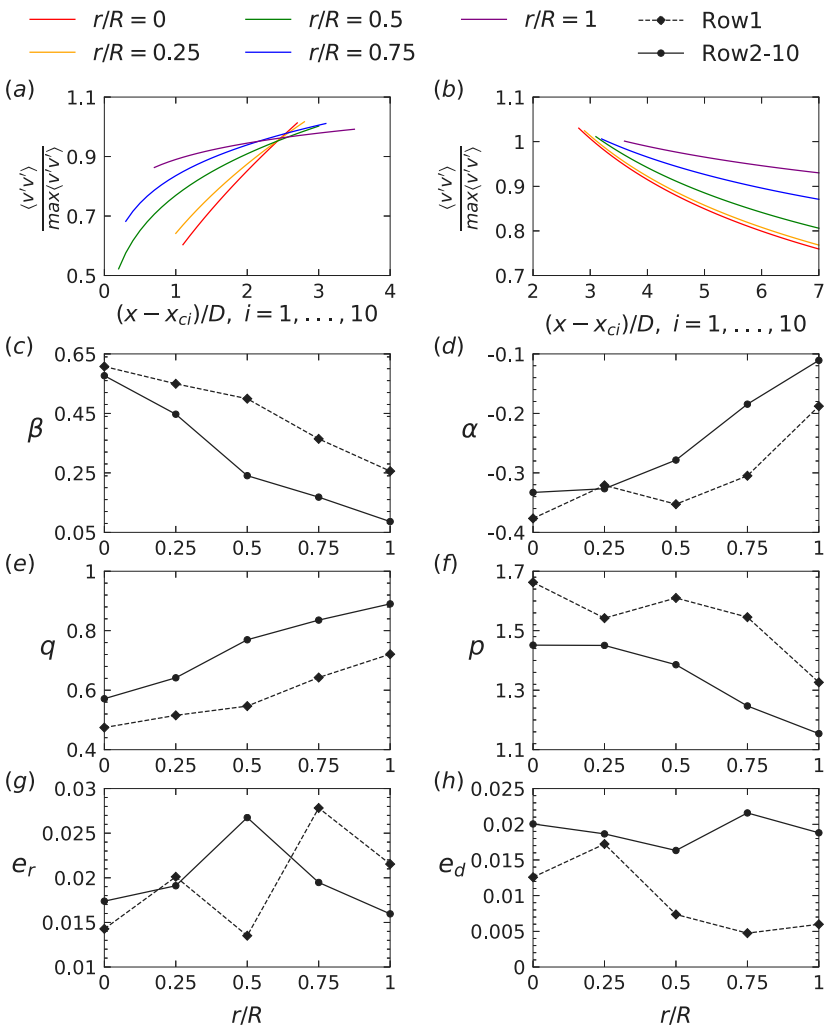

Fig. 5. Fitting results for the spanwise Reynolds normal stress for (a,b) the fitted curves for Row2-10, (c,d) exponents, (e,f) coefficients, and (g,h) errors. (a,c,e,g) are for the rise and (b,d,f,h) are for the decay, respectively.

spacings ($\Delta = 4, 5, 7, 8D$) are employed. The simulated wind turbines are the 2.5 MW Clipper wind turbine of the rotor diameter $D = 96$ m and the hub height of 80 m. The free-slip boundary condition is applied on the spanwise and top boundaries. The logarithmic law for rough wall is employed at the bottom boundary. At the inlet, three inflows with different roughness lengths, i.e., inflow1 with $k_s = 0.001$ m, inflow2 with $k_s = 0.01$ m and inflow3 with $k_s = 0.1$ m. The computational domain is $23D \times 7D \times 10.42D$ in the streamwise, spanwise and vertical directions respectively with the corresponding numbers of grid nodes $461 \times 281 \times 143$.

3. Results

In this section, we examine the similarity of the Reynolds normal stresses in Section 3.1, and propose and test the empirical formulae for their downstream evolutions in Sections 3.2 and 3.3.

3.1. Similarity of the Reynolds normal stresses

The similarity of the downstream variations of the Reynolds normal stresses is examined using the LES data of the Horns Rev wind farm.

In Figs. 1–3, the downstream variations of the Reynolds normal stresses are shown for different blade spanwise locations. Those plotted on the left (Figs. 1–3(a,c,e,g,i)) are normalized using the incoming wind speed U_0 at the corresponding spanwise position, while the right subfigures (Figs. 1–3(b,d,f,h,j)) are normalized by their maxima located in the range of $1D - 6D$ wind turbine downstream. For each row, the Reynolds normal stresses are averaged among wind turbines in the same row. Only the data on the horizontal plane located at the hub height are analyzed. For a nonzero blade spanwise position, the quantities are further averaged over both sides of the wake centerline. As seen, the variations of the Reynolds normal stresses are featured by two stages, i.e., a rise in the near wake and a following decay as moving further downstream, except for $r/R = 0$ where a secondary peak in the near wake due to the nacelle is identified.

We first examine Figs. 1–3(a,c,e,g,i). The rise in the near wake happens with the expansion of the tip shear layer, where the mixing

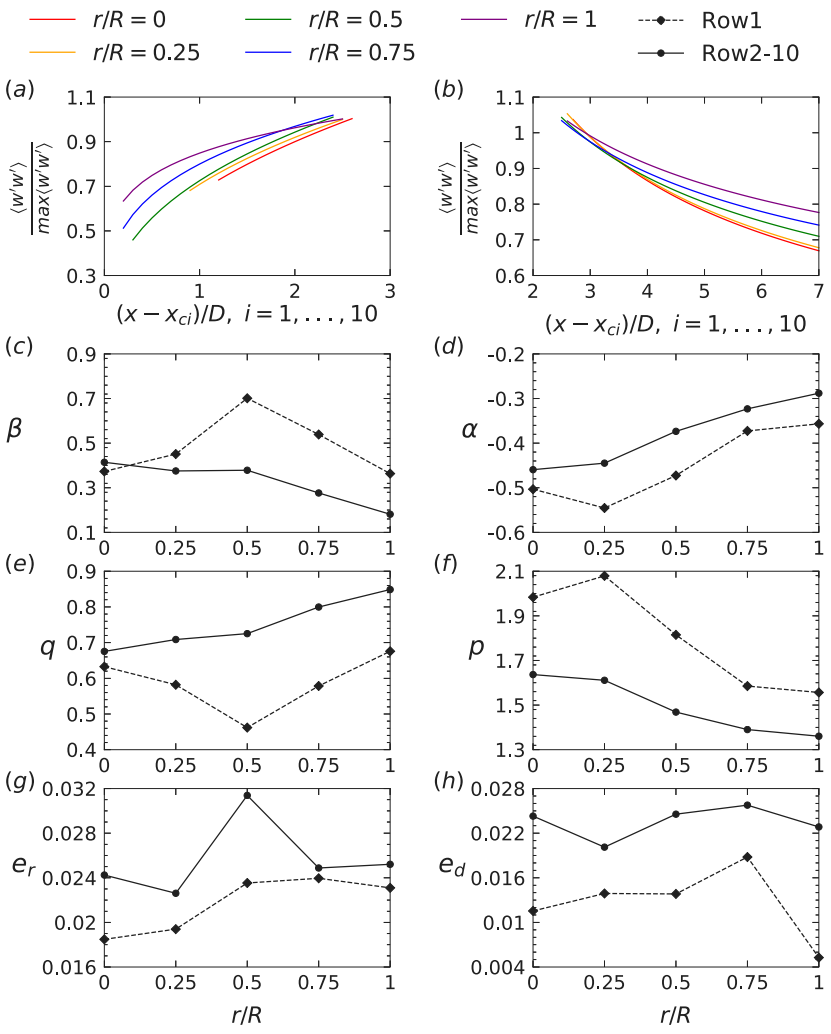

Fig. 6. Fitting results for the vertical Reynolds normal stress for (a,b) the fitted curves for Row2-10, (c,d) exponents, (e,f) coefficients, and (g,h) errors. (a,c,e,g) are for the rise and (b,d,f,h) are for the decay, respectively.

of the wake with the ambient flow occurs. The peaks locate at $1D$ to $4D$ turbine downstream locations. After the peak, the Reynolds normal stress decays, as the tip shear layer merges at the centerline and the velocity gradient gradually decreases. The peaks of the streamwise Reynolds normal stress locate closer to the wind turbine at the blade spanwise locations closer to the blade tip. For the spanwise component of the Reynolds normal stresses (Fig. 2), the peaks are close to the turbine at locations near the centerline. For the vertical component (Fig. 3), on the other hand, the locations of the peaks are roughly the same. The magnitudes of the maxima are higher at the near-tip locations for the streamwise Reynolds normal stress when compared with other locations, which, however, are lower for the other two components. As for the increase rate and the decay rate, they are observed being higher near the blade tip for the streamwise component, while being higher near the centerline for the other two components. We then examine Figs. 1–3(b,d,f,h,j) and find that the Reynolds normal stresses collapse with each other for Row2-10 (i.e. all the rows except the first one) when normalized using the corresponding maximum. At different blade spanwise positions, different trends are observed as shown in Figs. 1–3(a,c,e,g,i). It is noticed that the curves for the Row1 deviate from those of Row2-10 considerably as it faces the freestream instead of upstream wind turbine wakes.

3.2. Empirical formulae for Reynolds normal stresses

In this section, the empirical formulae for the downstream variations of the Reynolds normal stresses, which are normalized by the corresponding maximum, are fitted using a power function as follows,

$$F_{fit} = \begin{cases} q((x - x_{ci})/D)^{\beta}, \text{ for the rise,} \\ p((x - x_{ci})/D)^{\alpha}, \text{ for the decay,} \end{cases} \tag{3}$$

where q and p, and β and α are the coefficients and exponents to be fitted. Since the curves of Row1 are different from other rows, Row1 and Row2-10 are fitted separately. The fitting results are shown in Figs. 4–6 with the fitted curves shown in subfigures (a,b), the fitted coefficients and exponents in (c–f), and the fitting errors (which is the root-mean-square of $F - F_{fit}$) in (g–h).

Fig. 4 shows the fitting for the streamwise Reynolds normal stress. As seen, the fitted coefficient q gradually increases and the fitted

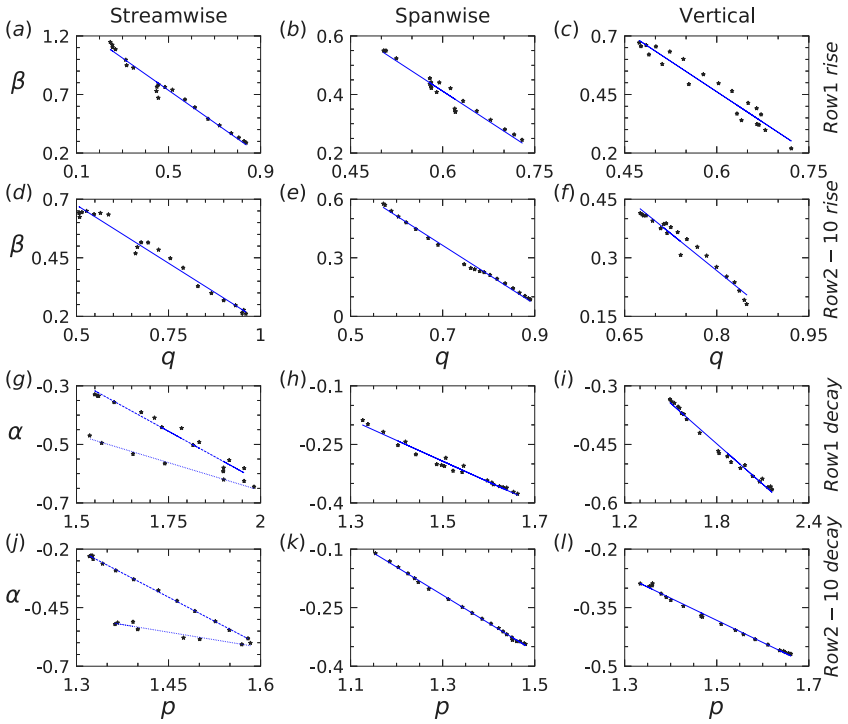

Fig. 7. Correlations between fitted exponents and coefficients. Black stars: the Horns Rev data; Blue lines: linear fit. For the streamwise Reynolds normal stress, two separate linear fits are observed for the decay portion.

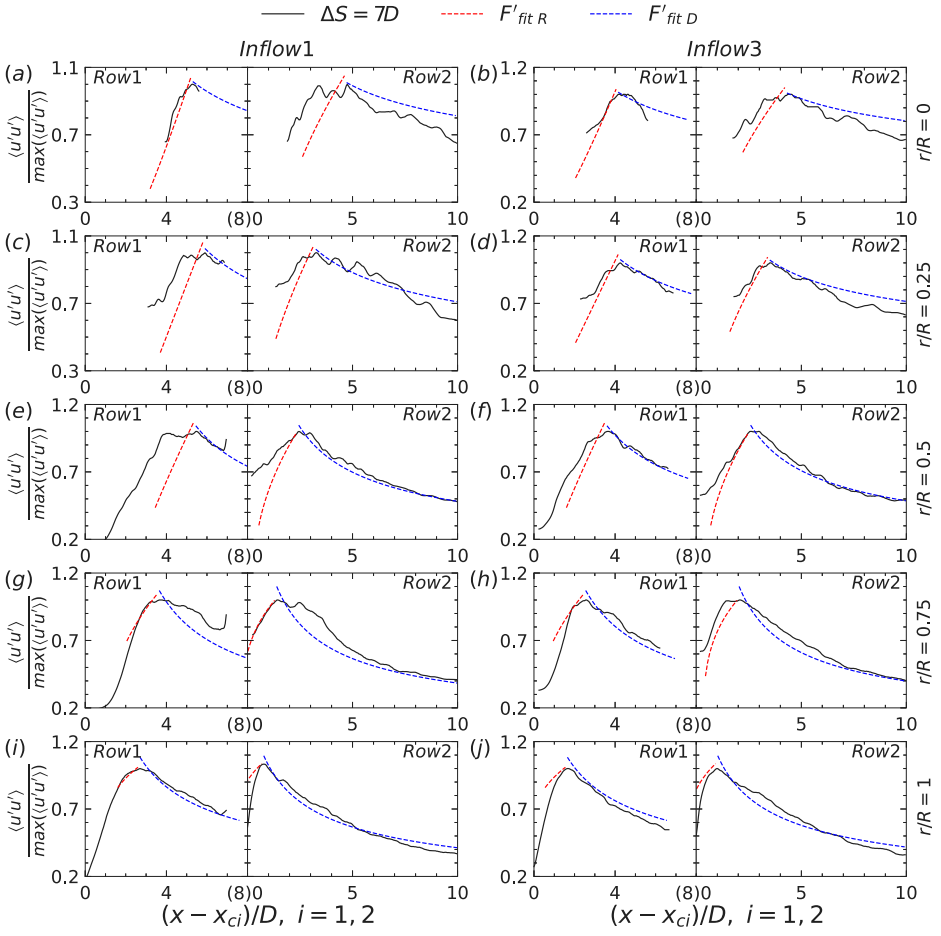

Fig. 8. Comparison of the normalized streamwise Reynolds normal stress from the empirical expression with the LES data of the two tandem turbine cases with different inflows (i.e., inflow1 $k_s = 0.001$ m, inflow3 $k_s = 0.1$ m) for the same turbine spacing $7D$.

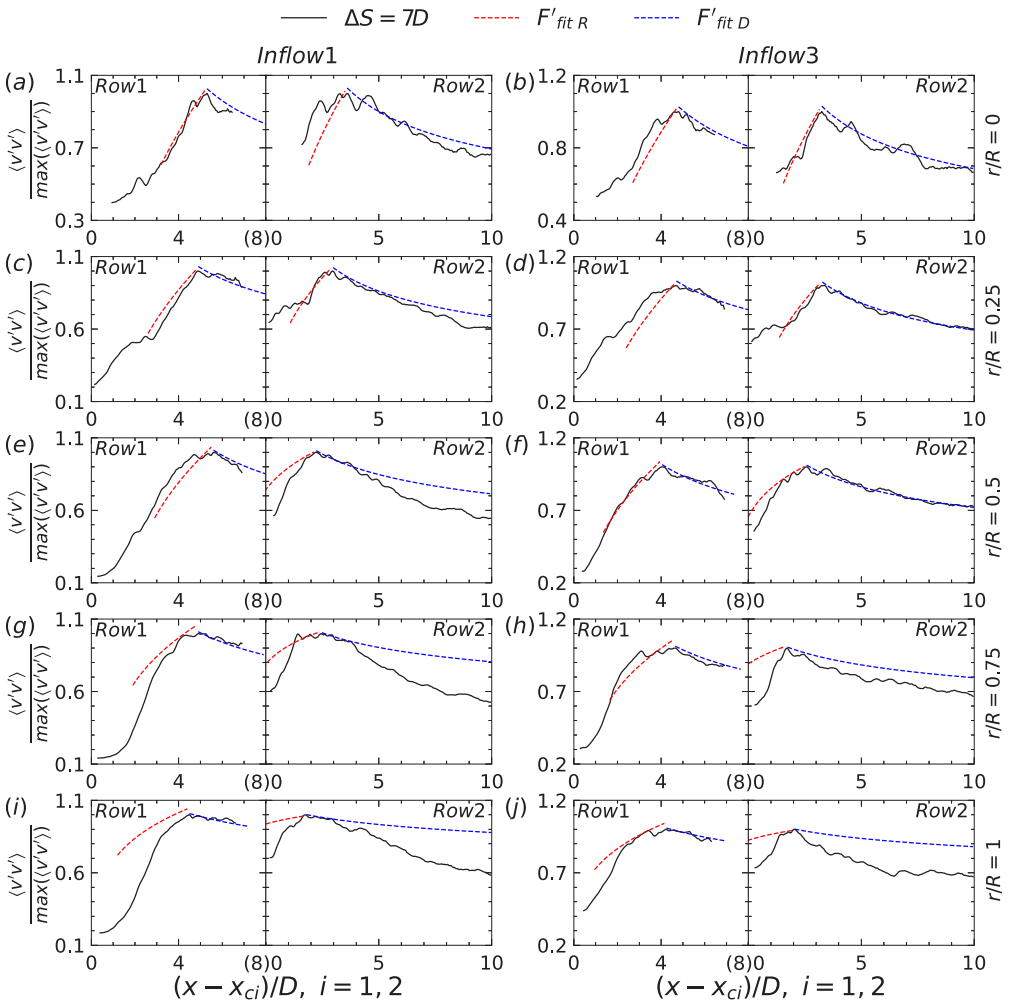

Fig. 9. Comparison of the normalized spanwise Reynolds normal stress from the empirical expression with the LES data of the two tandem turbine cases with different inflows (i.e., inflow1 $k_s = 0.001$ m, inflow3 $k_s = 0.1$ m) for the same turbine spacing $7D$.

exponent β decreases along the blade spanwise direction for the rise portion. For the decay portion, the fitted exponent α first decreases and then increases from $r = 0.75R$ for both Row1 and Row2-10, while the fitted coefficient p varies in the opposite way with a slightly different turning point for Row2-10. The errors are observed being smaller than 5% for both the rise and decay portions. It is interesting to notice that the overall variations of the coefficients and exponents for Row1 follow the same trends as Row2-10, although the inflows are different.

The fits for the spanwise and vertical Reynolds normal stresses are shown in Figs. 5 and 6. The overall variations of the fitted coefficients q and exponents β (for the rise portion) with r for the spanwise Reynolds normal stresses are similar with those for the streamwise component. For the vertical component of the Reynolds normal stresses, the fitted q and β for Row1 first decrease and increase with r until $r = 0.5R$, respectively, being different from Row2-10, then follow the same trends as Row2-10 (as observed for the other two components of the Reynolds normal stresses). As for the decay portion, the overall variations of the fitted p and α are similar for the spanwise and vertical Reynolds normal stresses, showing a roughly increase and decrease with r respectively. The errors (e) are small (<5%) for all the three components, indicating the fitness of the empirical formulae.

After fitting the empirical formulae for the Reynolds normal stresses at different blade spanwise positions, here we examine the correlations between the fitted exponents and coefficients to facilitate further application of the proposed expressions. In order to reveal the correlation between the exponent and the coefficient, more blade spanwise positions in addition to $r/R = 0, 0.25, 0.75, 1.0$ are selected and fitted using the Horns Rev data. Fig. 7 shows the exponent vs. the coefficient from the fitted curves at different blade spanwise positions for Row1 and Row2-10 and different components of the Reynolds normal stresses. A linear relation between the exponent and the coefficient is observed for almost all cases except for the decay portion of the streamwise component of the Reynolds normal stresses, for which two linear relations appear. Careful examination of the plotted data points shows that the two linear relations are related to two different ranges of blade spanwise positions, one for the region near the centerline and the other for the near-tip region, with the dividing point in the range of $r \in [0.5R, 0.75R]$, and the one with higher magnitude of slope for the region near the centerline. The slopes (k) and the corresponding

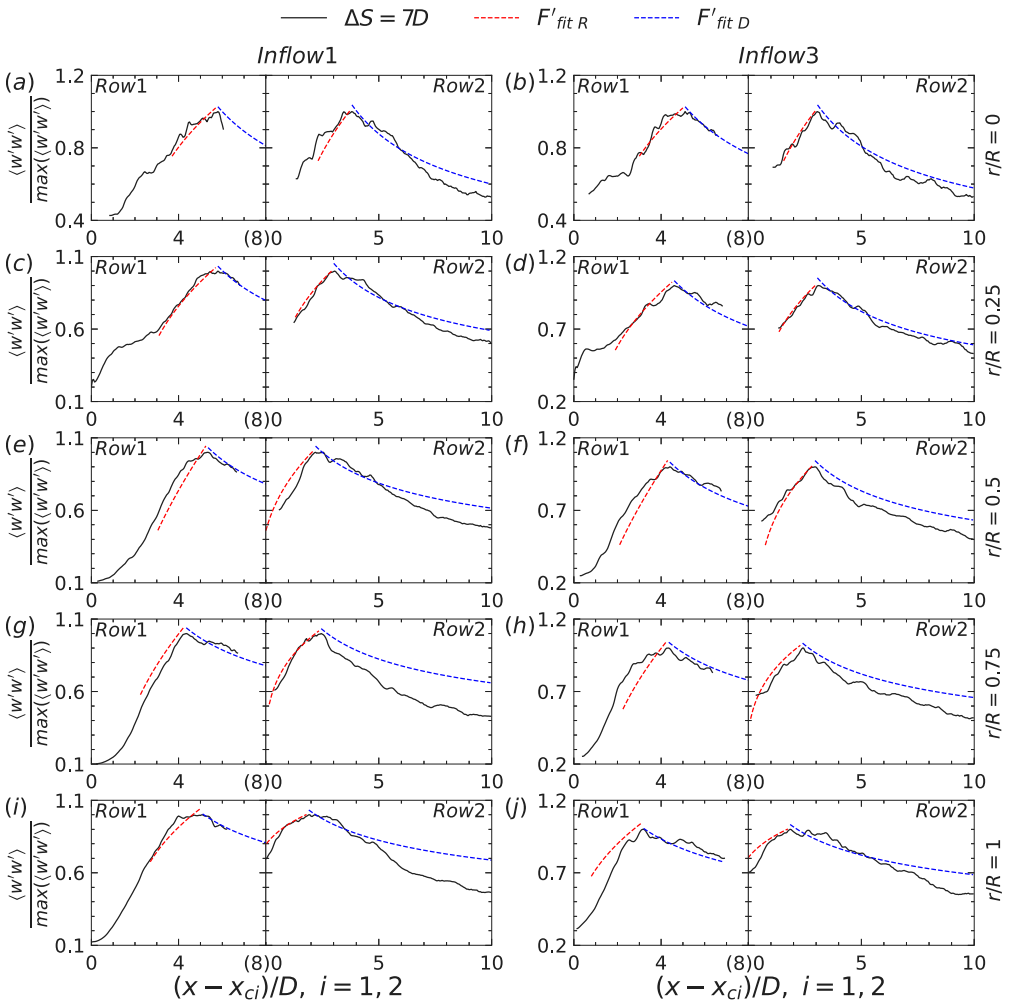

Fig. 10. Comparison of the normalized vertical Reynolds normal stress from the empirical expression with the LES data of the two tandem turbine cases with different inflows (i.e., inflow1 $k_s = 0.001$ m, inflow3 $k_s = 0.1$ m) for the same turbine spacing $7D$.

Table 1
The slopes (k) and the corresponding intercepts (c) of the linear relation.

	Streamwise		Spanwise		Vertical	
	k	c	k	c	k	c
Row1 rise	−1.38	1.42	−1.37	1.23	−1.73	1.50
Row2-10 rise	−0.99	1.17	−1.51	1.42	−1.27	1.28
Row1 decay	−0.69 −0.38	0.75 0.10	−0.53	0.51	−0.35	0.17
Row2-10 decay	−1.37 −0.43	1.58 0.07	−0.72	0.72	−0.57	0.47

intercepts (c) of the linear relation ($\beta = kq + c$ or $\alpha = kp + c$) are summarized in Table 1.

Hence, the parameters to be fitted in the empirical expression can be reduced to one as the exponent and coefficient are not independent, making it more convenient for use.

3.3. Test of the empirical formulae for Reynolds normal stresses

In this section, the fitted empirical formulae are tested using the LES data of the two tandem wind turbine cases with four different downwind spacings and three different inflows [17]. For the sake of brevity, several representative comparisons are selected and showed in Figs. 8–13. It should be noted that the comparisons were made only for the rise and decay portions of the Reynolds normal stresses, without concerning their variations in the very near wake. As the locations for the maxima of the Reynolds normal stresses do not coincide with those of the Horns Rev wind farm, the wind turbine downstream distance x in the empirical formulae (Eq. (3)) fitted in Section 3.2 is translated by $x_m - x_m^t$ before evaluation, where x_m^t is the turbine downstream distance of the maximum for the test case, and x_m the turbine downstream distance of the maximum for the Horns Rev case.

In Figs. 8–10, the fitted empirical formulae are evaluated using the cases with different inflows (inflow1 and inflow3). It is seen that the proposed formulae in general capture the streamwise variations of the LES data. For the streamwise component of the Reynolds normal stresses shown in Fig. 8, the curves from the empirical expression

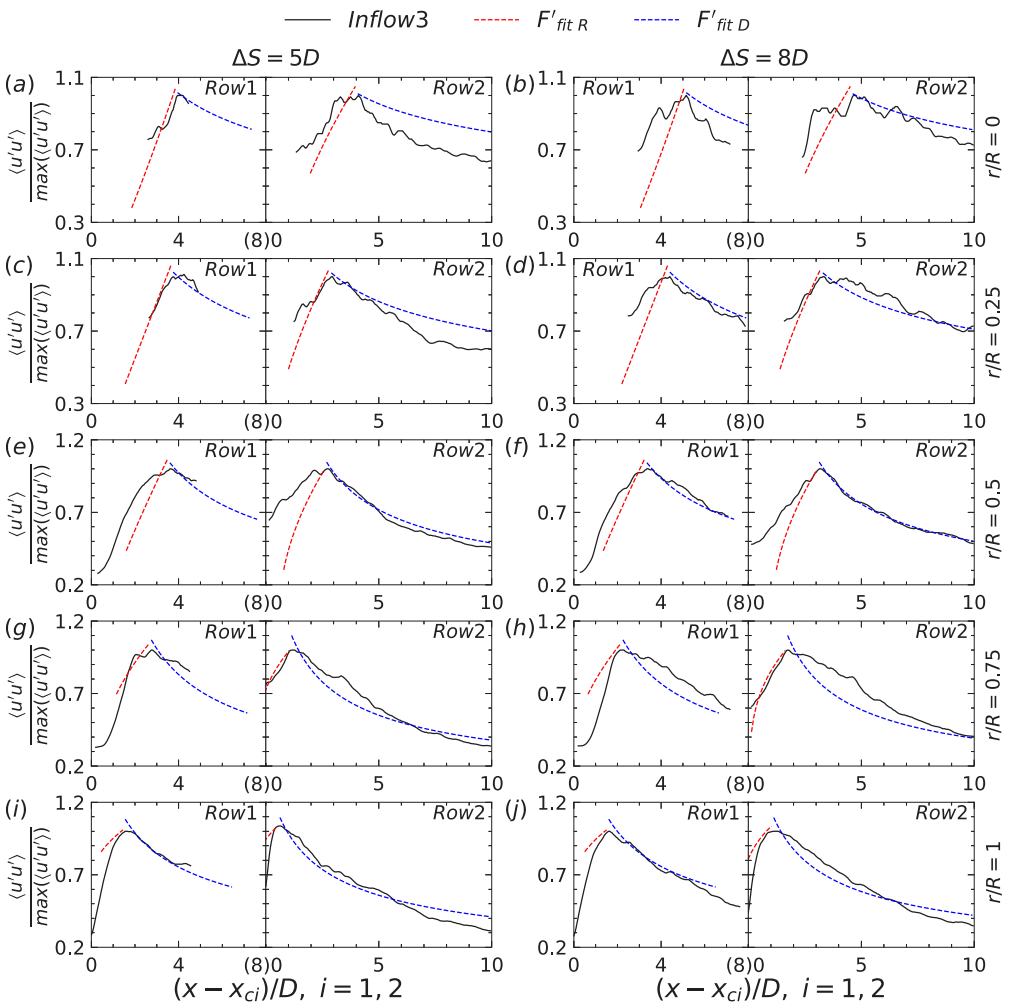

Fig. 11. Comparison of the normalized streamwise Reynolds normal stress from the empirical expression with the LES data of the two tandem turbine cases with different turbine spacings (i.e., $5D$, $8D$) under inflow3 $k_s = 0.1$ m.

collapse well with the LES data in the decay portion for both inflows. For the rise portion, discrepancies are observed for the low inflow turbulence intensity case (inflow1) especially in the interior region of the blade (e.g., $r/R = 0.25, 0.50$). As for the spanwise component (Fig. 9), discrepancies are observed in the outer part of the blade ($r/R > 0.5$) for both the rise and decay portions, that the empirical formulae underestimate the rise and decay rates. In the inner part of the blades ($r/R \leq 0.5$), on the other hand, an overall good agreement is achieved for both rise and decay portions for both inflows. For the vertical component, discrepancies are mostly observed in the decay portion in the outer part of the blade (Fig. 10). It is noticed that the data employed for fitting only cover the wake until $6D$ turbine downstream. This is one possible reason for the larger discrepancies observed in the far wake for some plots.

Figs. 11–13 show the results for the cases with different downwind spacings ($5D$, $8D$) for the same inflow (inflow3). For the case with $5D$ downwind spacing, the comparison of the decay of Row1 is not shown for the spanwise and vertical components as they hardly decrease at the allowable turbine downstream locations. It is seen in Fig. 11 for the streamwise component that the results from the empirical formulae in general agree well with the LES results except for Row2 in the $\Delta S = 5D$ case at the locations near the centerline ($r/R = 0, 0.25$) for the decay portion. For the spanwise and vertical components, good agreements are observed at locations near the centerline (e.g., $x/R = 0, 0.25$). Discrepancies are observed at locations near the tip for the decay portion (e.g., $r/R = 0.75, 1$ for $\Delta S = 5D$). Overall, the curves from the empirical expression agree well with the LES data for the $\Delta S = 8D$ case. A better performance is observed for the streamwise component when compared with the other two components.

Since the empirical formulae are fitted to Reynolds normal stresses normalized using their maximum values, it is essential to know the maxima and the corresponding downstream locations (x_m) for their practical applications. Fig. 14 presents the two quantities from the HR and two tandem wind turbine cases for different blade spanwise positions. For the streamwise component, the maximum generally increases and the corresponding position moves gradually closer to the wind

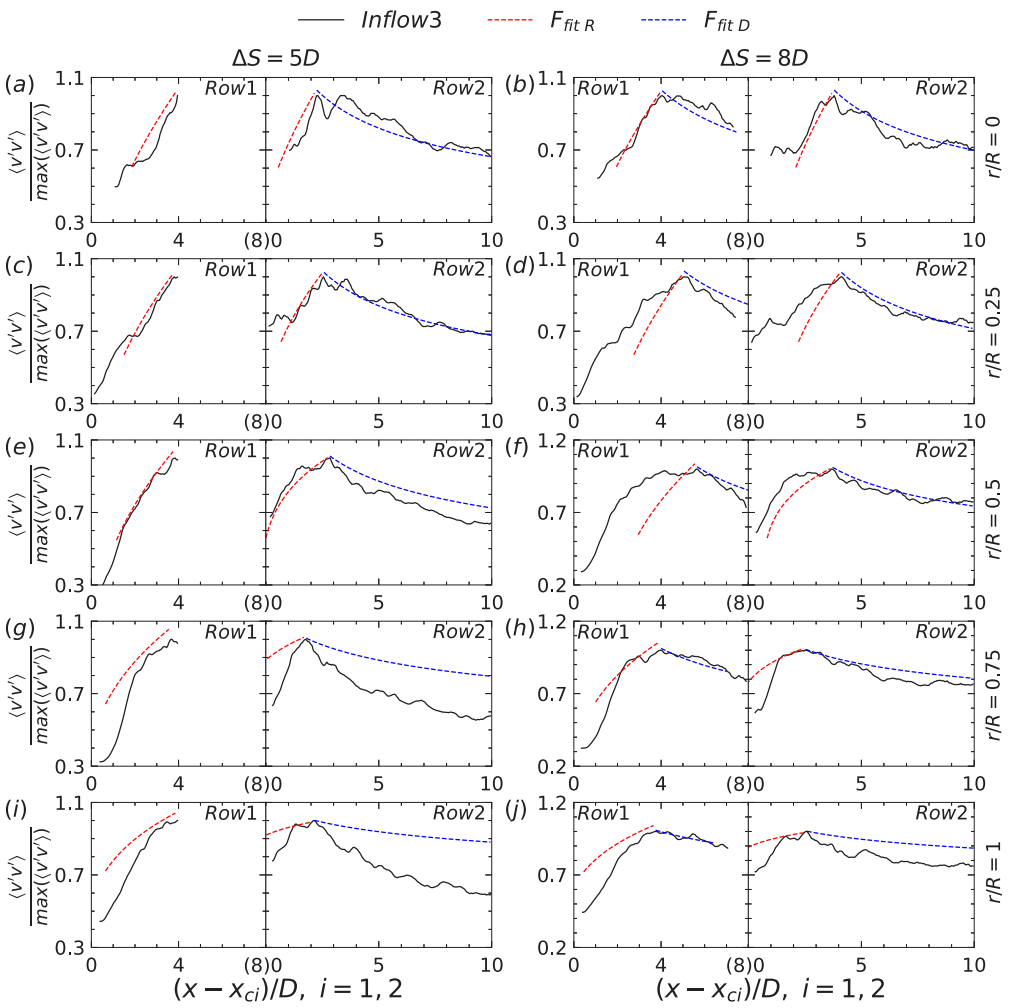

Fig. 12. Comparison of the normalized spanwise Reynolds normal stress from the empirical expression with the LES data of the two tandem turbine cases with different turbine spacings (i.e., $5D$, $8D$) under inflow3 $k_s = 0.1$ m.

turbine as the radial distance from the wake centerline (r) increases for almost all cases. The variations of the maxima for the vertical component and the x_m of the spanwise and vertical components, on the other hand, do not follow a general trend.

Overall, the evaluation results show that the fitted empirical formulae can capture the streamwise variations of the Reynolds normal stresses in an acceptable way, especially for the streamwise component, e.g., the decay fitting curves of Row2 almost overlap with the LES data, such as at $r = 0.5R$, the inflow1 case with $7D$ spacing and the inflow3 case with $5D$, $8D$ spacing for streamwise, etc. This not only shows the usefulness of the proposed empirical formulae, but also indicates that the similarity of the downstream variations of the Reynolds normal stresses probably exist for a wide range of inflows and wind turbine spacings.

4. Conclusions

In this paper, we investigated the similarity of the Reynolds normal stresses, proposed empirical formulae to describe their downwind variations at different blade spanwise positions using the LES data of the Horns Rev wind farm, and tested the proposed empirical formulae using the LES data from two tandem wind turbine cases.

The results show that the downwind variation curves of the Reynolds normal stresses for wakes of Row2-10 collapse well with each other when normalized using the corresponding maximum, indicating the similarity of the Reynolds normal stress for waked wind turbine wakes. The empirical expressions are obtained by fitting a power function for the rise and the decay portions separately. Trends as a function of the blade spanwise position are observed for the fitted coefficients, exponents, and the maximum and its corresponding turbine downwind position. Furthermore, linear relations are observed for the negatively correlated exponent and coefficient of the empirical formulae. The test results show that the empirical formulae can capture well the downstream variations of the streamwise Reynolds normal stress for different downwind wind turbine spacings and different inflows. Some discrepancies were observed for the other two components especially at locations near the blade tip.

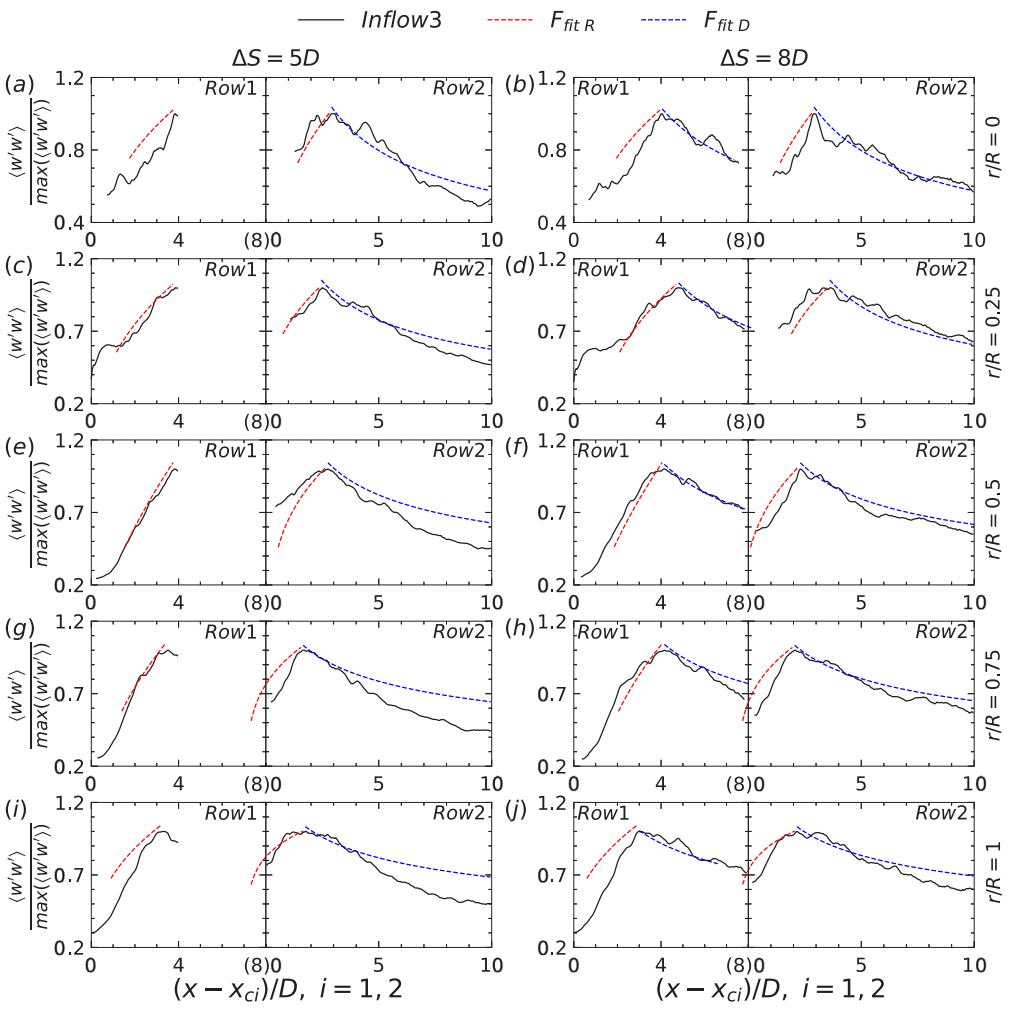

Fig. 13. Comparison of the normalized vertical Reynolds normal stress from the empirical expression with the LES data of the two tandem turbine cases with different turbine spacings (i.e., $5D$, $8D$) under inflow3 $k_s = 0.1$ m.

In order to apply the proposed empirical formulae to actual wind energy applications, the maxima of the Reynolds normal stresses ($\max\langle u_i' u_i' \rangle$) and the corresponding wind turbine downwind positions (x_m) are required. On the one hand, if rough estimations are desired, the values of $\max\langle u_i' u_i' \rangle$ and x_m from the current study can be utilized. On the other hand, if more precise predictions are needed, models for $\max\langle u_i' u_i' \rangle$ and x_m must be developed. However, the streamwise evolution of $\langle u_i' u_i' \rangle$ is related to a complicated process including the breakdown of tip vortices, the interaction between the hub vortex and the tip shear layer, and the wake meandering, and is affected by many factors such as the inflow, the wind turbine's operating regimes, the blade design, etc. Consequently, developing a model for $\max\langle u_i' u_i' \rangle$ and x_m requires systematic research and will be tackled in future work using methods like machine learning to handle the complexity of the issue.

CRediT authorship contribution statement

Yi Zhang: Conceptualization, Investigation, Methodology, Writing – original draft. **Zhaobin Li:** Methodology, Software, Writing – review & editing. **Xiaohao Liu:** Methodology, Data acquisition, Writing – review & editing. **Fotis Sotiropoulos:** Methodology, Software, Writing – review & editing. **Xiaolei Yang:** Conceptualization, Methodology, Software, Writing – review & editing.

Declaration of competing interest

The authors declare that they have no known competing financial interests or personal relationships that could have appeared to influence the work reported in this paper.

Acknowledgments

This work was funded by the NSFC Basic Science Center Program for "Multiscale Problems in Nonlinear Mechanics" (NO. 11988102), National Natural Science Foundation of China (NO. 12172360), Institute of Mechanics CAS, and Chinese Academy of Sciences, China.

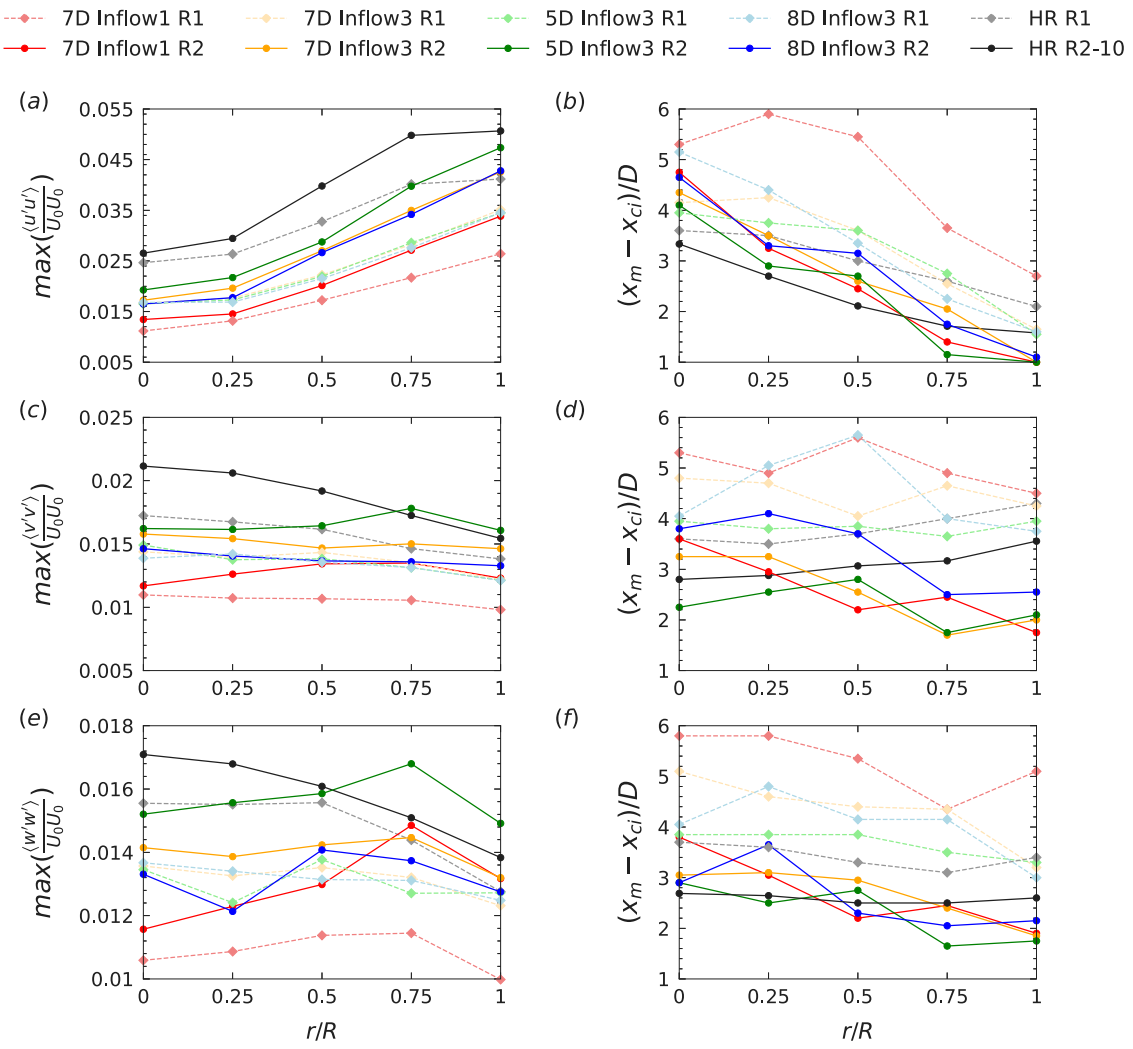

Fig. 14. The maxima and the corresponding turbine downstream positions of the Reynolds normal stresses for Horns Rev wind farm and two tandem wind turbine cases. Black lines represent the Horns Rev wind farm case, and the other color lines represent two tandem wind turbine cases. (a,b) the streamwise, (c,d) the spanwise, and (e,f) the vertical. R represents Row in the legend.

References

[1] R.J. Barthelmie, K. Hansen, S.T. Frandsen, O. Rathmann, J.G. Schepers, W. Schlez, J. Phillips, K. Rados, A. Zervos, E.S. Politis, P.K. Chaviaropoulos, Modelling and measuring flow and wind turbine wakes in large wind farms offshore, Wind Energy 12 (5) (2009) 431–444.

[2] R.J. Barthelmie, L.E. Jensen, Evaluation of wind farm efficiency and wind turbine wakes at the Nysted offshore wind farm, Wind Energy 13 (6) (2010) 573–586.

[3] F. Porté-Agel, M. Bastankhah, S. Shamsoddin, Wind-turbine and wind-farm flows: A review, Bound.-Lay. Meteorol. 174 (2020) 1–59.

[4] X. Yang, F. Sotiropoulos, A review on the meandering of wind turbine wakes, Energies 12 (24) (2019) 4725.

[5] L. Vermeer, J. Sørensen, A. Crespo, Wind turbine wake aerodynamics, Prog. Aerosp. Sci. 39 (6) (2003) 467–510.

[6] C. Meneveau, Big wind power: seven questions for turbulence research, J. Turbul. 20 (1) (2019) 2–20.

[7] U. Högström, D.N. Asimakopoulos, H. Kambezidis, C.G. Helmis, A. Smedman, A field study of the wake behind a 2 MW wind turbine, Atmos. Environ. 22 (4) (1988) 803–820.

[8] A. Crespo, J. Herna´ndez, Turbulence characteristics in wind-turbine wakes, J. Wind Eng. Ind. Aerodyn. 61 (1) (1996) 71–85.

[9] A. Duckworth, R. Barthelmie, Investigation and validation of wind turbine wake models, Wind Eng. 32 (5) (2008) 459–475.

[10] I. Neunaber, M. Hölling, R.J.A.M. Stevens, G. Schepers, J. Peinke, Distinct Turbulent Regions in the wake of a wind turbine and their inflow-dependent locations: The creation of a wake map, Energies 13 (20) (2020).

[11] T. Ishihara, G.-W. Qian, A new Gaussian-based analytical wake model for wind turbines considering ambient turbulence intensities and thrust coefficient effects, J. Wind Eng. Ind. Aerodyn. 177 (2018) 275–292.

[12] L. Li, Z. Huang, M. Ge, Q. Zhang, A novel three-dimensional analytical model of the added streamwise turbulence intensity for wind-turbine wakes, Energy 238 (2022) 121806.

[13] M. Bastankhah, F. Porté-Agel, A new analytical model for wind-turbine wakes, Renew. Energy 70 (2014) 116–123.

[14] L. Li, Z. Huang, M. Ge, Q. Zhang, A novel three-dimensional analytical model of the added streamwise turbulence intensity for wind-turbine wakes, Energy 238 (2022) 121806.

[15] D. Foti, X. Yang, L. Shen, F. Sotiropoulos, Effect of wind turbine nacelle on turbine wake dynamics in large wind farms, J. Fluid Mech. 869 (2019) 1–26.

[16] Z. Li, X. Yang, Large-eddy simulation on the similarity between wakes of wind turbines with different yaw angles, J. Fluid Mech. 921 (2021) A11.

[17] X. Liu, Z. Li, X. Yang, D. Xu, S. Kang, A. Khosronejad, Large-eddy simulation of wakes of waked wind turbines, Energies 15 (8) (2022).

[18] X. Yang, F. Sotiropoulos, R.J. Conzemius, J.N. Wachtler, M.B. Strong, Large-eddy simulation of turbulent flow past wind turbines/farms: the Virtual Wind Simulator (VWiS), Wind Energy 18 (12) (2015) 2025–2045.

[19] X. Yang, F. Sotiropoulos, A new class of actuator surface models for wind turbines, Wind Energy 21 (5) (2018) 285–302.

[20] M. Germano, U. Piomelli, P. Moin, W.H. Cabot, A dynamic subgrid-scale eddy viscosity model, Phys. Fluids A 3 (7) (1991) 1760–1765.

[21] X. Yang, X. Zhang, Z. Li, G.-W. He, A smoothing technique for discrete delta functions with application to immersed boundary method in moving boundary simulations, J. Comput. Phys. 228 (20) (2009) 7821–7836.

[22] L. Ge, F. Sotiropoulos, A numerical method for solving the 3D unsteady incompressible Navier–Stokes equations in curvilinear domains with complex immersed boundaries, J. Comput. Phys. 225 (2) (2007) 1782–1809.

[23] D.A. Knoll, D.E. Keyes, Jacobian-free Newton–Krylov methods: a survey of approaches and applications, J. Comput. Phys. 193 (2) (2004) 357–397.

[24] Y. Saad, A flexible inner-outer preconditioned GMRES algorithm, SIAM J. Sci. Comput. 14 (2) (1993) 461–469.